Design and Optimization for a Novel 3D Flux Micro-machine used in Trajectory Correction Fuze

Jianghai Hui, Min Gao, Chaowang Li, Zhifei Ke

Abstract—This paper proposed a novel permanent magnet machine with 3D flux path for the trajectory correction fuze, which is used to correct the projectile's trajectory during flight. First, the topology structure and equivalent magnetic circuit model were described, and the 3D flux path was portrayed. To conduct the torque and generated power optimization, the geometric parameters which influence the performance were found out by the relationship between the geometric parameters and performance. Second, the machine's flux-concentrating effect and magnetic distribution were achieved. The breaking torque, load voltage and stator current were also acquired by preliminary simulation with finite element model. Based on the sample points produced by orthogonal design and the range analysis results, the three approximation models were created, from which the Kriging model was selected to represent the simulation. Third, non-dominated sorting genetic algorithm II and multi-objective particle swam optimization were adopted to optimize the breaking torque and generated power. The optimal performance and the corresponding geometric parameters were acquired after optimization by the algorithms. In addition to this, to compare the optimization results from the two optimization algorithm and verify their correctness, the breaking torque and generated power under five different speed discrepancy with respect to the projectile's flight velocity were obtained by simulation based on the optimized machine's model. Finally, the prototype experiment was conducted to verify the optimization method and simulation. The results indicated that the proposed machine which had been optimized can meet the performance acquirement of trajectory correction.

Index Terms—machine; breaking torque; generated power; design of experiment; approximation model; Non-dominated sorting genetic algorithm II; multi-objective particle swam optimization

I. INTRODUCTION

Guided ammunition, also named smart artillery munitions, is meant to be a precision location strike system and have excellent accuracy of impact due to the delicate design of the inner mechanical and electronic components. During last 40 years, the US Army has developed a kind of guidance control system that contains sophisticated embedded electronic devices and an actuating mechanism. A kind of trajectory correction fuze showed in Fig. 1, which was firstly introduced in 2006 by the USA in their patent, two-dimension guidance of projectile fixed wings, is one kind of such guidance system. Generally, the electronic devices in the fuse powered by power source control the spin of the fixed canards tied to the fuze, thus changing the aerodynamic characteristics of the projectile during flight and realizing precision guidance for it. As the power source and operator in the fuse, the electrical machine plays an important role during the whole operation process.

Fig. 1. Projectile equipped with trajectory correction fuze

Due to the limitation for fuze's available space, the design targets of the machine which include miniaturization, high torque and power density should be taken into consideration. Compared with the traditional electrically excited machine, the permanent magnetic machine has advantage of flexibility of topology structure design. According to the flux direction, the permanent magnetic machine can falls into three general categories: radial flux, axial flux and transverse flux. Earlier, the radial flux PM was applied to most area. However, the torque of the radial flux PM cannot be promoted efficiently for the limitation between stator slot and teeth. The transverse flux permanent magnetic machine firstly proposed in the late 80s, last century solved such problem produced by the radial flux PM [1]. The ring coil is used so that the limitation mentioned above can be released. The TFPMM's stator slot is vertical to the winding thus realizing the decoupling of the electrical circuit and magnetic circuit and promoting the

torque effectively. In addition, the topology structure can be smart designed thus making TFPMM (transverse flux permanent magnet machine) very suitable the limited available space of trajectory correction fuze.

Many different topologies structure of TFPMM were researched and had been designed. The claw-pole and flux-concentrating transverse flux permanent magnetic machine whose permanent magnetic are embedded in the rotor has been introduced in the literature [2-6], Besides, the double-side E-Core transverse flux machine which has a cylindrical rotor, sandwiched between E-core stators on both sides has been also designed and analyzed [7-12]. In addition, Jia Z. et al proposed a novel transverse flux permanent magnet motor with double-C stator hoops. The power density was significantly increased due to the flux-concentrated rotor [13-14]. Yan et al. presented a kind of novel flux switching transverse flux permanent magnet wind generator and proposed a novel flux concentrated transverse flux permanent magnet disk generator for low speed direct drive wind power applications [15-16]. Zhang H. et al. proposed and analyzed a new bidirectional cross-linking transverse flux permanent magnet synchronous motor which can fully utilize the rotor permanent magnets and have larger space utilization ratio than the traditional transverse flux machine [17-18]. Yao et al. designed a concentrated-flux transverse flux permanent magnet motor based on a completed design of a surface mounted transverse flux permanent magnet motor with auxiliary stators [19].

Besides, the new materials, such as SMC (soft magnetic composites), were used for some novel topologies which were originally made from the surface-insulated silicon electrical steel [20-23]. The advantages of the SMC, compared with the traditional silicon electrical steel, are the isotropy and low eddy current losses [24]. However, in gun-launched projectiles, large shock loadings both in axis and transverse direction generated during a launch process tend to cause the sophisticated devices to fail. Therefore, the SMC is not suitable for the micro-machine in fuze due to its low mechanical strength. In this paper, the surface-insulated silicon steel sheet is considered.

To design a kind of micro-machine which can meet the torque requirement of the trajectory correction fuze, this paper proposed a novel 3D flux micro-machine whose topology structure and the magnetic equivalent circuit model are described primarily. Then, the relation between the machine's geometric parameters and performance is established, the magnetic distribution of machine and performance including breaking torque and generated power are obtained by primarily simulation with FEM (finite element model). Subsequently, an optimization is conduct to acquire the optimal machine' design parameters with the DOE (design of experiment) method, approximation model and the two optimization algorithms, NSGA-II (Non-dominated Sorting Genetic Algorithm II) and MOPSO (Multi-objective Particle Swam Optimization). Furthermore, the optimized machine is remodeled and simulated with FEM to verify whether the performance indexes meet the acquirement or not.

The remainder of this paper is organized as follows: Sect.2 presents the description of this machine's design, including topology structure and magnetic equivalent circuit model. Sect.3 establishes the relation between the performance and machine's geometry parameters, determining the optimization variables and objectives. Sect.4 carries out a preliminary simulation with FEM of machine to acquire the breaking torque and generated power. Sect.5 conducts an optimization process for the performance. In sect.6, we conclude the paper.

II. PROPOSED MICRO-MACHINE'S DESCRIPTION

A. Operation process

The machine plays an important role in the fuze which controls the revolution of fixed canards to change the projectile aero-dynamical characteristics, thus realizing the projectile's trajectory correction during flight. The fixed canards showed in Fig. 2(a) are in a high-speed revolution reversed to the projectile (See the black arc-shaped arrow line in Fig. 2(b)), forming speed discrepancy between the canards and projectile. According to the principle of trajectory correction, the steady speed discrepancy can achieve the correction for the projectile's flight trajectory. Therefore, as Fig. 2 shows, the breaking torque produced by the machine must ensure the canards in a balanced state when the projectile comes into correction period. Lots of live firing tests results indicated that the breaking torque must be 20% higher than wind resistance moment imposed on the canards during flight. In addition, the machine also serves as the power source for the electrical device in the fuze, ensuring the fuze's normal work.
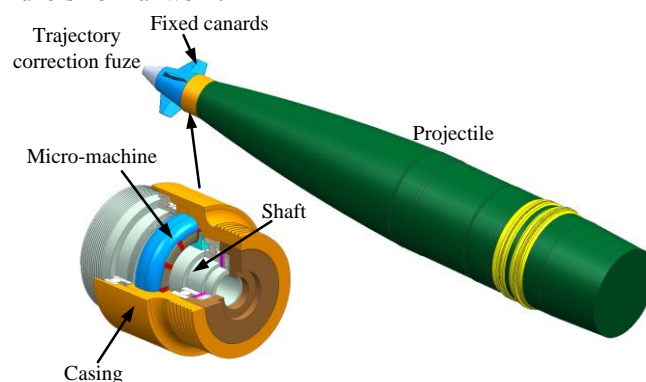
(a) Schematic diagram of the machine in the fuze
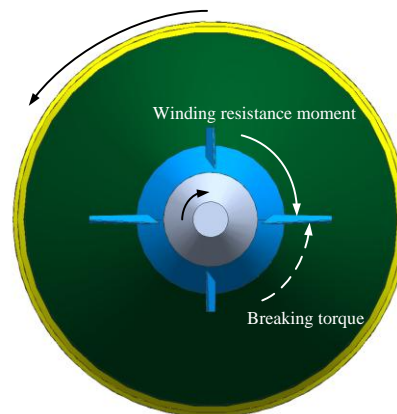
(b) Schematic diagram of speed discrepancy
Fig. 2. Schematic diagram for the trajectory correction principle

B. Structure

Fig. 3 exhibits the proposed machine comprised of a stator mounted to the shaft and a passive rotor fixed to the casing.

The PMs (permanent magnets) mounted with the stator and arranged in flux concentrating manner, which the magnetization direction for each adjacent magnet is magnetized in opposite direction. The winding consist of ring coil is inserted in the stator slot. As mentioned above, in order to ensure the strength of the machine subjected to impact loads during launch, the stator and rotor are all made from the silicon steel sheets manufactured by rolling. Hence the rotor yoke and teeth, the stator yoke and pole are integrated, letting the whole machine's structure compact and reliable.
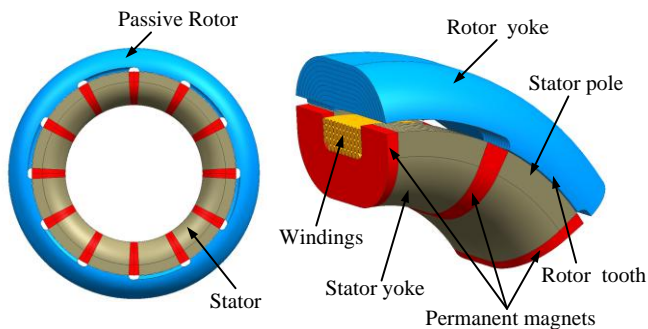

Fig. 3. Structure and configuration of proposed micro-machine

C. Magnetic equivalent circuit and operating principle
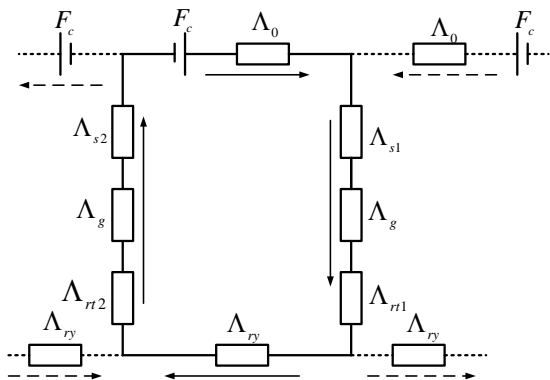

Fig. 4. 3D path of the flux

Distinguished from the axial, radial, and transverse flux permanent magnetic machine, the path of this proposed machine's magnetic circuit is not on a single plane. However, it is depicted as a 3D path. Fig. 5 draws the machine's flux path which begins with N pole of one PM and end with S pole of this PM, passing stator pole, gap, rotor tooth, rotor yoke, another rotor tooth, gap, and another stator pole. The magnetic equivalent circuit is showed in Fig. 4 with respect to the flux path showed in Fig. 5. In the figure, F_c refers to the magnetic motive force source. Λ_0 is the PM's inner permeability. Λ_{s1}、Λ_g、Λ_{rt1}、Λ_{ry}、Λ_{rt2}、Λ_{s2} donate the relative permeability of stator pole, gap, rotor tooth, rotor yoke, another rotor tooth and another stator pole, respectively. The induced electromotive force is produced by changing of flux linkage direction due to the rotor's high speed revolution relative to stator. One side, the induce electromotive force supplies power for others device in the fuze. Another side, the torque produced from machine can be employed as breaking torque to control the revolution speed of the fixed canards during flight.
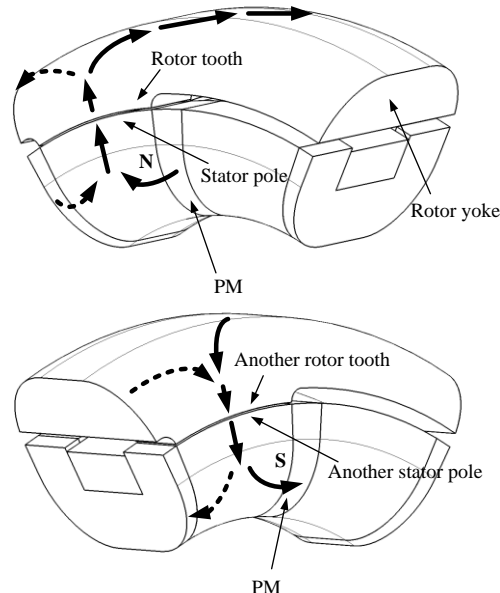

Fig. 5. 3D path of the flux

III. GEOMETRIC PARAMETERS DETERMINATION

The machine's performance is determined by its size which can be deduced based on the given characteristics of performance. With help of the relation between the size parameters and performance, researchers can conduct optimization for the size to reach the optimum performance of the machine. There is no identical math expression to describe such relation for 3D flux permanent magnetic machine because of so many different topology structures. In this section, base on the general math expressions about the machine's performance, we deduce the formulas to find out the size parameters which influence this kind of machine's torque performance.

TABLE I EXPLANATIONS OF GEOMETRIC PARAMETERS

Parameter	Explanation
D_{si}	Inner diameter of stator
D_{so}	Outer diameter of stator
b	Width of stator slot
h	Height of stator slot
c	Height of stator yoke
l_1	Circumferential length of stator pole
l_2	Circumferential length of PM
l_3	Circumferential length of rotor teeth
a	Width of stator pole Width of rotor teeth
e	Height of rotor teeth
L	Axial length of the whole machine
D_o	Outer diameter of the whole machine
D_i	Inner diameter of the whole machine
α_p	Arc coefficient of machine
δ	Air gap thickness

In the first, the geometric marking of the machine's structure is exhibited in Fig. 6, and the explanations for each parameter are listed in Table I.
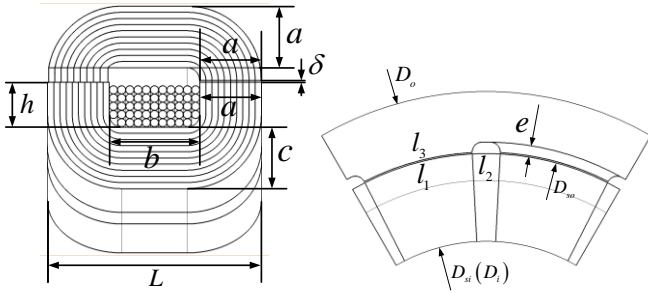
Fig. 6. Geometric marking of the machine's structure

The general machine's induced electromotive force E, Electromagnetic power P and torque T are described by the following equations:

$$E = 4.44 fNpk_N \Phi \tag{1}$$

$$P = EI \cos\varphi \tag{2}$$

$$T = \frac{P}{\omega} = \frac{4.44 fNpk_N I\Phi \cos\varphi}{2\pi f} = 0.707 Npk_N I\Phi \cos\varphi \tag{3}$$

Where f donates the machine's mechanical revolution frequency. N is the winding turns. P, k_N, and I are the number of pole-pairs, winding factor, and the phase current, respectively. $\cos\varphi$ refers to the power factor influenced by the load property. Furthermore, Φ donates the flux amplitude of air gap in a single pole which can be expressed as:

$$\Phi = B_g S_1 \tag{4}$$

Where B_g is the flux density amplitude of air gap. S_1 donates the area of the stator pole which is represented by:

$$S_1 = al_1 \tag{5}$$

Similarly, the area of the rotor pole S_2 can be written as:

$$S_2 = al_3 \tag{6}$$

In this paper, the pole pitch in this machine cannot be defined according to the traditional machine's definition. Therefore, We can define the pole pitch τ and the arc coefficient of machine α_p in this machine by the equations in the following:

$$\tau = l_1 + l_2 = \frac{\pi D_{so}}{2p} \tag{7}$$

$$\alpha_p = l_1 / \tau \tag{8}$$

Letting $\mathrm{rad}\, l_1$ and $\mathrm{rad}\, l_2$ represent the radian of the circumferential length of stator pole and PM, respectively, thus l_1 and l_2 can be represented as:

$$l_1 = \frac{\mathrm{rad}\, l_1}{2} D_{so} = \frac{\pi D_{so}}{2p}\alpha_p \tag{9}$$

$$l_2 = \frac{\mathrm{rad}\, l_2}{2} D_{so} = \frac{\pi D_{so}}{2p}(1-\alpha_p) \tag{10}$$

It has been mentioned in the previous section that the stator and rotor are laminated by steel sheet which fabricated by rolling. Therefore, the limited relation among those dimensional parameters of the machine is given by:

$$\begin{cases} a = c \\ D_i = D_{si} \\ L = 2a + b \\ D_{so} = D_i + (L-b) + 2h \\ D_o = D_{so} + 2\delta + 2e + (L-b) \end{cases} \tag{11}$$

Based on equation (4), the relation between the machine's performance and size can be established. The torque T and power P can be further modified into:

$$\begin{cases} P = 1.11\pi fk_N NB_g I\alpha_p \left[D_o - 2\delta - 2e - (L-b) \right](L-b)\cos\varphi \\ T = 0.177\pi k_N NB_g I\alpha_p \left[D_o - 2\delta - 2e - (L-b) \right](L-b)\cos\varphi \end{cases} \tag{12}$$

From equation (12), the geometric parameters which influence the performance of the machine can be find out. The machine's outer diameter D_o and axial length L are constrained by the available space of the fuze's casing and shaft. Furthermore, the stator's slot width b, the winding turns N, height of the rotor teeth e and the arc coefficient α_p have great influence on the torque and power. Those four geometry parameters are served as the optimization variables and are given the initial value and range primarily which are summarized and listed in Table II. Besides, the determined geometric parameters are listed in Table III.

TABLE II GEOMETRY VARIABLES TO OPTIMIAZE

Optimization variable	Initial value	Value range (Single value)
b / mm	5	$4 \leq b \leq 7$
N	53	51,52,53,54
e / mm	1	$0.5 \leq r \leq 2$
α_p	0.8	$0.5 < \alpha_p < 0.95$

TABLE III DETERMINED GEOMETRIC VARIABLES

Design variable	Value
D_o / mm	54
L / mm	14.5
δ / mm	0.1
h /mm	2.65

IV. PRELIMINARY SIMULATION WITH FEM

To confirm the machine's flux-concentrating effect and the distribution of magnet, the FEM (finite element model) is established and simulated. Except for the parameters has been determined, the four design parameters listed in Table III could be chosen a initial design value. In this way, the rotating speed initially set is 10000 rpm. The machine's solid model simplified to be a one period and FEM are showed in Fig. 7. With simulation completed, magnetic field's vector in one of the stator poles and surface magnetic flux density have been portrayed and showed in Fig. 8 and Fig. 9. The effect flux-concentrating effect is clearly and the form of magnet vectors got from those figures indicates that the reasonable primarily design for the machine.
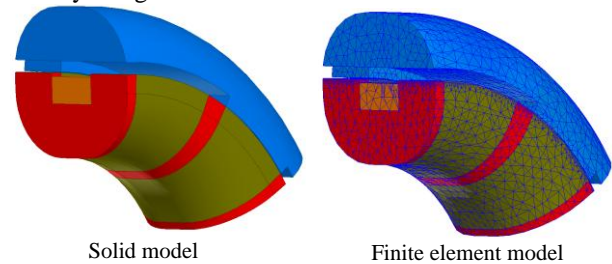

Solid model   Finite element model
Fig. 7. Machine's simplified solid model and FEM

The breaking torque, load voltage and stator current can be acquired through simulation, whose curve in one electric period is depicted in Fig.10. The value of the breaking torque can be divided into two parts: one part is the positive number

and another is the negative number. The negative values indicate the torque's direction is identical with the machine's revolution, thus promoting revolution. While the positive values indicate the torque's direction is reverse to the machine' revolution, that's the breaking torque. Calculated the average of the curve's value, the breaking torque is -0.3157 N·m . On the basis of the load voltage and stator current's curve in Fig. 10(b) and (c), Calculated the machine's generated power is 337.825W.
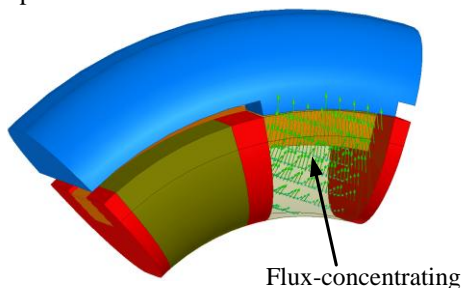

Fig. 8. Magnetic field's vector

TABLE IV Wind resistance moment corresponding to different flight velocity

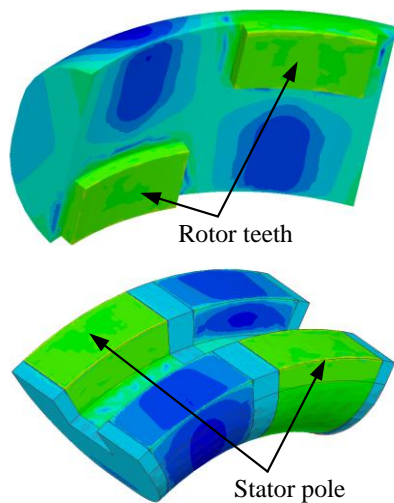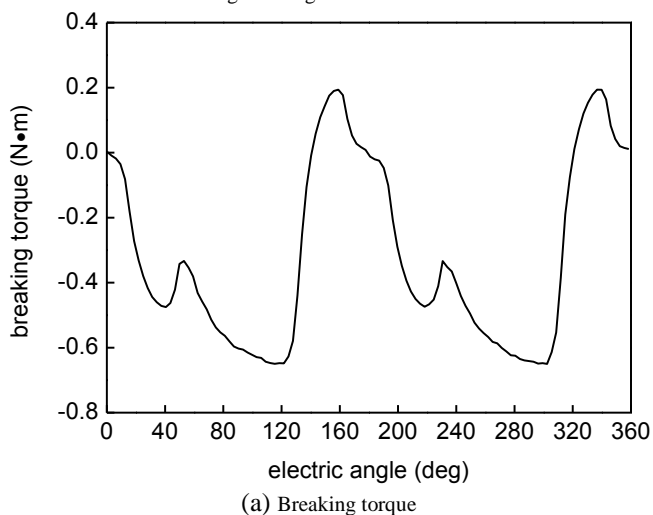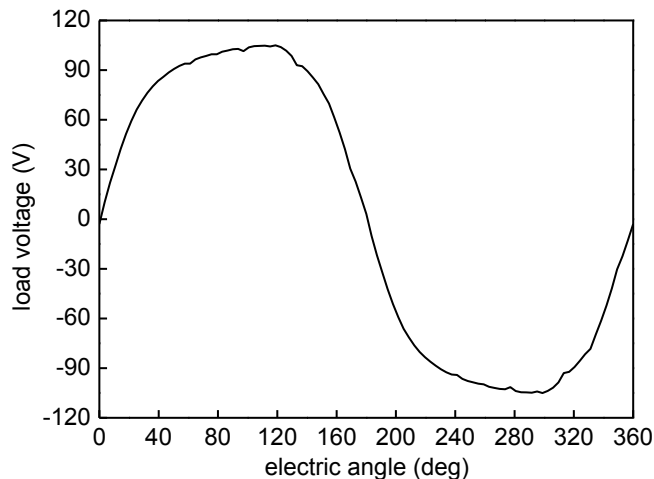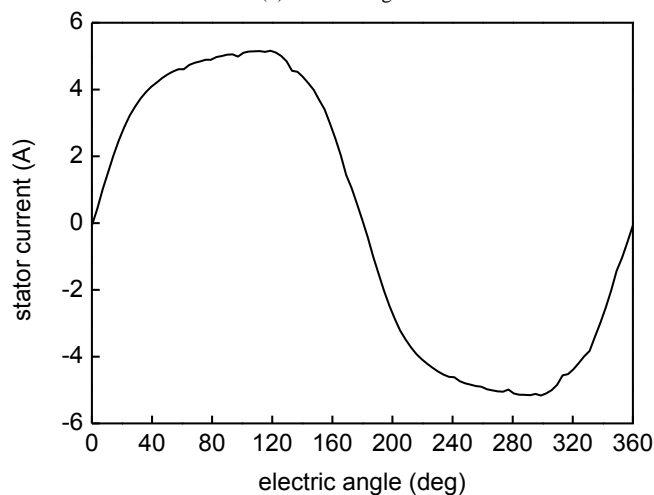| Flight velocity (Ma)	Speed discrepancy (rpm)	Wind resistance moment (N·m)
0.5	4200	0.185
0.7	6000	0.315
0.8	8000	0.393
1.0	10000	0.487
1.2	12000	0.674

Fig. 9. Magnet distribution

(a) Breaking torque

(b) Load voltage

(c) Stator current

Fig. 10. Electrical indexes for machine of initial design

As previous illustration in Sect.2, the machine must output the breaking torque 20% higher than the wind resistance moment so as to implement the trajectory correction for the projectile. The wind resistance moment corresponding to the speed discrepancy under the different flight velocity is showed in Table IV. It can be clearly seen from the table that the initial machine's breaking torque is less than the wind resistance moment whose value is 0.487 N·m under 1.0Ma flight velocity. Accordingly, the torque must be optimized to meet the requirement of trajectory correction. Furthermore, as the power source for the other electric device in the fuze, the machine's generated power must be over 300W, while the generated power worked out from the simulation results of the machine initial designed has reached this requirement. Accordingly, those two performance indexes will be regarded as the optimization objectives, and the four design variables listed in Table II are served as the optimization variables. In the next section, an optimization process is conducted to achieve the optimized breaking torque and generated power with respect to the optimal geometric variables.

V. MULTI-OBJECTIVES OPTIMIZATION

Derivation previously indicates the relation between the torque and geometric parameters while it must be noted that the torque optimization cannot be conducted with the only equations which contribute to narrow the geometric

parameters' scope. There are two optimization objectives and four variables to be optimized, thus a multi-objectives optimization will be conducted in this section. FEA (finite element analysis) would be applied for the whole optimization process including DOE (design of experiment), creating approximation model and optimization based on GA.

A. Design of experiment

Among the DOE method, including the full factorial design, orthogonal design, central composite design and Latin hypercube design are in common use. Orthogonal design which performs a fractional experiment to maintain orthogonal among the various factors and interactions will be adopted for the optimization in this section. The orthogonal design which can avoid a costly full-factorial experiment uses specific combinations of factors at different levels to greatly reduce the number of designs and still obtain meaningful factor effect information. In this optimization issue, the four variables are extracted as four factors and four levels for each parameter according to Table IV.

TABLE IV FACTORS AND LEVELS

Level	Factor			
	b / mm	N	e / mm	α_p
1	4	51	0.5	0.6
2	5	52	1	0.7
3	6	53	1.5	0.8
4	7	54	2	0.9

TABLE V ORTHOGONAL ARRAY AND SIMULATION RESULTS

Sample points	Factor				Performance index	
	b	N	e	α_p	T / N·m	P / W
1	1	1	1	1	-0.1044	285.734
2	1	2	2	2	-0.5143	334.49
3	1	3	3	3	-0.2513	317.485
4	1	4	4	4	-0.023	319.502
5	2	1	2	4	-0.2634	360.202
6	2	2	1	3	-0.3705	356.005
7	2	3	4	2	-0.1248	352.834
8	2	4	3	1	-0.1961	370.594
9	3	1	3	2	-0.0988	335.078
10	3	2	4	1	-0.1559	273.751
11	3	3	1	4	-0.1307	285.561
12	3	4	2	3	-0.5998	282.606
13	4	1	4	3	-0.5394	338.022
14	4	2	3	4	-0.165	344.114
15	4	3	2	1	-0.0937	322.82
16	4	4	1	2	-0.5528	305.255

The orthogonal array generated by 16 sample points and the corresponding simulation results are established as Table V shows. The FEM corresponding to each sample points are established and simulated with FEA to achieve the breaking torque and generated power. Each simulation is set for the condition of 10000 rpm revolution speed. Furthermore, the range analysis is carried out to obtain the effect of the variable on the two performance indexes. With each parameter's average value in different levels corresponding to each performance index calculated, the variables' effect tendency on machine's performance with the level can be worked out. Take width of stator slot b for example, in level i (i =1, 2, 3, 4) its average value $t_{ij}(N_s)$ corresponding to machine's breaking torque (performance index j, j =1, 2) can be calculated as follows:

$$t_{11}(b) = \frac{1}{4}\left[x_1(b) + x_2(b) + x_3(b) + x_4(b)\right] = -0.225$$

Similarly, in the other three levels, its average value corresponding to the breaking torque can also be obtained by:

$$t_{21}(b) = \frac{1}{4}\left[x_5(b) + x_6(b) + x_7(b) + x_8(b)\right] = -0.239$$

$$t_{31}(b) = \frac{1}{4}\left[x_9(b) + x_{10}(b) + x_{11}(b) + x_{12}(b)\right] = -0.246$$

$$t_{41}(b) = \frac{1}{4}\left[x_{13}(b) + x_{14}(b) + x_{15}(b) + x_{16}(b)\right] = -0.338$$

The range value $R_j(N_s)$ (j =1, 2, 3) for winding turns corresponding to breaking torque is presented by:

$$R_1(N_s) = \max\left[t_{11}(N_s), t_{21}(N_s), t_{31}(N_s), t_{41}(N_s)\right]$$
$$- \min\left[t_{11}(N_s), t_{21}(N_s), t_{31}(N_s), t_{41}(N_s)\right]$$
$$= 0.113$$

Accordingly, the average value of the slot width corresponding to the machine's generated power can also be calculated and the other three variables' analysis results can be achieved by the same method.

All the variables' average values are presented by the line chart showed in Fig. 11 which can visualize the effect tendency of each variable on the two performance indexes with the level changed.
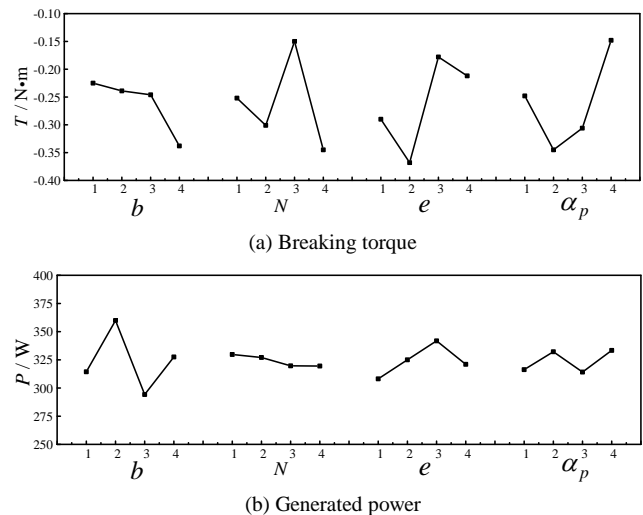

(a) Breaking torque

(b) Generated power

Fig. 11 The variables' effect tendency on performance indexes with the level

From the line chat it is apparently seen that the effect tendency of each variable for the breaking torque and generated power. However, those lines cannot indicate the changing law of the variables' effect on the performance. Therefore, based on the results of orthogonal design's sample points, it is necessary to create the approximation model to represent the nonlinear relation between the machine's performance indexed and the four variables.

B. Approximation modeling

Among approximation model, including RSM (response surface model)，RBF neural network and Kriging model are in common use. To select the approximation model which can better predict the simulation results, the coefficient of determination which is a measure of the amount of reduction in the variability of the response variables obtained using the estimation coefficients in the model is adopted and defined in the follows:

$$R^2 = 1 - \frac{\sum_{i=1}^{n}(y_i - \hat{y}_i)^2}{\sum_{i=1}^{n}(y_i - \overline{y})^2} \qquad (13)$$

Where y_i and $\hat{y}_i$ donate the simulation value and predicted value, respectively. $\overline{y}$ refers to the average value of the simulation results of sample points. In general, the value of R^2 must be over 0.9.

The variables and performance in the sample points should be non-dimensioned before approximation by the equations in the following:

$$\begin{cases} x_1 = b/4 \\ x_2 = N/50 \\ x_3 = e/1 \\ x_4 = \alpha_p \end{cases} \quad \begin{cases} y_1 = T/-0.5844 \\ y_2 = P/300 \end{cases} \qquad (14)$$

Furthermore, ten ample points are collected as test point randomly, and the distribution of predicted value generated by RSM, RBF neural network and Kriging technique relative to simulation value are depicted in the scatter diagram as Fig. 12, 13 and 14 show.
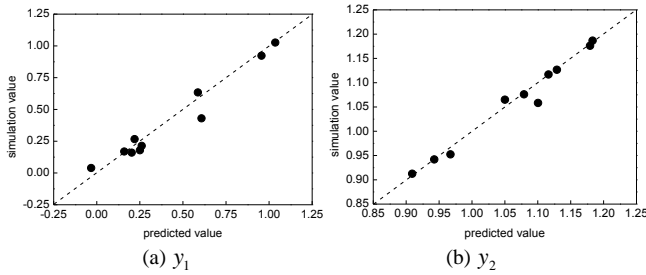

(a) y_1 (b) y_2

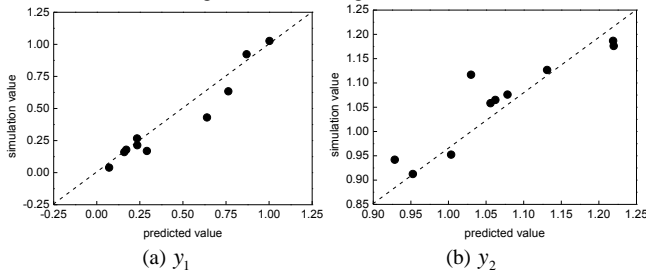Fig. 12. Scatter diagram of RSM

(a) y_1 (b) y_2

Fig. 13. Scatter diagram of RBF neutral network
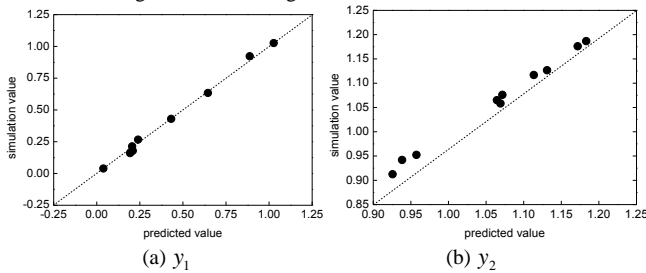

(a) y_1 (b) y_2

Fig. 14. Scatter diagram of Kriging model

The value of R^2 of the three approximation model are calculated by equation (13), the results are listed in Table VI.

TABLE VI R^2 FOR APPROXIMATION MODEL

	RSM	RBF	Kriging
y_1	0.95136	0.92312	0.99531
y_2	0.97322	0.82371	0.99516

It can be apparently seen from the scatter diagrams that the predicted value generated by Kriging model is closer to simulation value than the RSM and RBF neutral work. The coefficient value R^2 listed in Table VI can also testify the result. The value of objective y_2 generated by RBF neutral work is less than 0.9, thus the model cannot be used for the further optimization. Accordingly, Kriging model can be the approximation model to represent the simulation model which is used for the next step of the performance optimization.

C. Optimization with algorithm

Because there are two performance indexes regarded as two optimization objectives, there is no explicit optimization design for the generator with the best value of all the objectives. Pareto solutions can be used for multi-objectives optimization which have many outstanding designs making good tradeoff among those objectives exist. In this part, on the basis of the approximation created in the previous section, the Pareto solutions for generator's optimization will be searched with two kinds of algorithm, MOPSO and NSGA-II. In addition, it should be noted that the final solutions achieved by the algorithm may be not the optimum solutions and selection of an appropriate index to evaluate the quality of the solutions is not a simple task. Accordingly, we will conduct a comparison of the two optimum solutions from the two kinds of algorithm.

The optimization mathematical model based on the performance indexes can be presented by:

$$maximum: \begin{cases} y1 = f(x1, x2, x3, x4) \geq 1 \\ y2 = f(x1, x2, x3, x4) \geq 1 \end{cases}$$

$$subject: \begin{cases} 1 \leq x1 \leq 1.75 \\ 1.02 \leq x2 \leq 1.08 \\ 0.5 \leq x3 \leq 2 \\ 0.6 < x4 \leq 0.9 \end{cases} \qquad (15)$$

MOPSO mimics the social behavior of animal groups such as flocks of birds or fish shoals. The process of finding an optimal design point is likened to the food-foraging activity of these organisms. Particle swarm optimization is a population-based search procedure where individuals (called particles) continuously change position (called state) within the search area. In other words, these particles 'fly' around in the design space looking for the best position. The best position encountered by a particle and its neighbors along with the current velocity and inertia are used to decide the next position of the particle. The optimization with MOPSO can be described by:

Given dimension of search space whose value is W, the number of particles n, the position of particle i can be written by $x_i = (x_{i1}, x_{i2}, \cdots, x_{iW})$, and the best position of particle i from the beginning to now is expressed by $pbest_i = (p_{i1}, p_{i2}, \cdots, p_{iW})$. The best position of the whole population from the beginning to now can be presented by $gbest_i = (g_{i1}, g_{i2}, \cdots, g_{iW})$.

The velocity of particle i is written by $v_i = (v_{i1}, v_{i2}, \cdots, v_{iW})$, therefore the particle's velocity and position in each dimension can be expressed in the following:

$$\begin{cases} v_{iw}(t+1) = v_{iw}(t) + c_1 \times r_1 \times \left[p_{iw}(t) - x_{iw}(t) \right] \\ \qquad + c_2 \times r_2 \times \left[p_{gw}(t) - x_{gw}(t) \right] \\ x_{iw}(t+1) = x_{iw}(t) + v_{iw}(t+1) \end{cases} \quad (16)$$

$$(1 \le i \le n, \quad 1 \le w \le W)$$

Where c_1 and c_2 are the learning factors. r_1 and r_2 are the random numbers. The initial position and velocity of the particle swarm are yielded randomly, and the optimum solutions are acquired by interaction according to equation (25).

The MOPSO is an extension of PSO algorithm for the multi-objectives optimization whose flowchart is shown in Fig. 15. As for the optimization of generator performance, given the maximum interaction is 100, and the initial number of particle is 100. With algorithm searching completed, 10,000 result points which are on behalf of 10,000 solutions are obtained. Furthermore, 1,840 of those points constitute the Pareto front depicted in scatter diagram shown in Fig. 13.
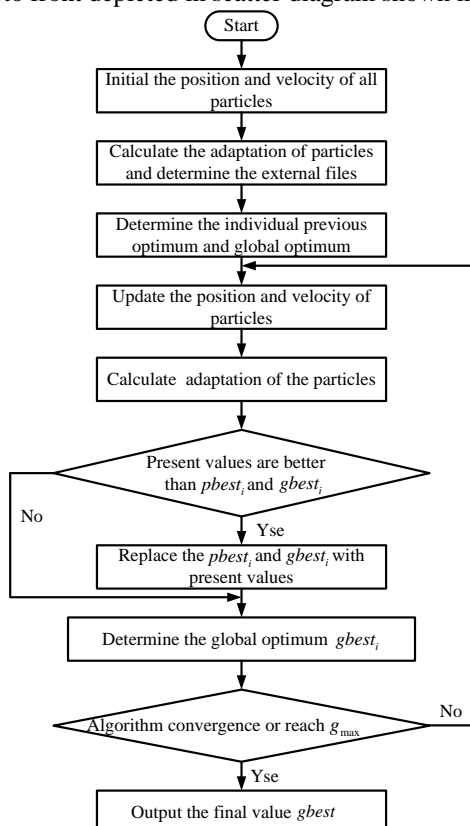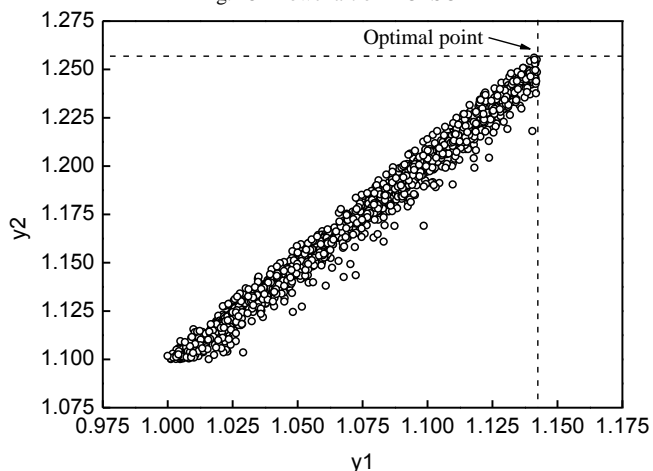

Fig. 15 Flowchart of MOPSO

Fig. 16 Scatter diagram of Paroto front by MOPSO

The best solution selected from Pareto front depicted by the scatter diagram according to the optimization target principle as equation (15) shows. The best solution is summarized in Table VII.

TBALE VII BEST SOLUTION BY MOPSO

Optimization variable	Dimensionless	Real value
b	1.116	4.464
N	1.06	52
e	1.335	1.335
α_p	0.812	0.812

In the Non-dominated Sorting Genetic Algorithm (NSGA-II), each objective parameter is treated separately. Standard genetic operation of mutation and crossover are performed on the designs. Selection process is based on two main mechanisms, "non-dominated sorting" and "crowding distance sorting". By the end of the optimization run a Pareto set is constructed where each design has the "best" combination of objective values and improving one objective is impossible without sacrificing one or more of the other objectives. The flowchart of NSGA-II is showed as Fig. 17.
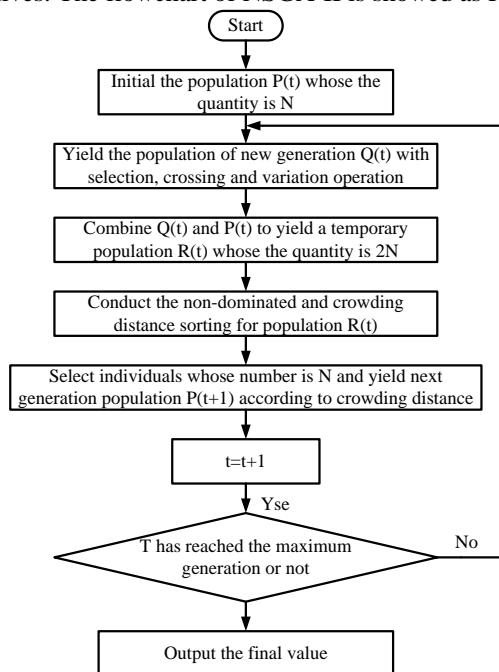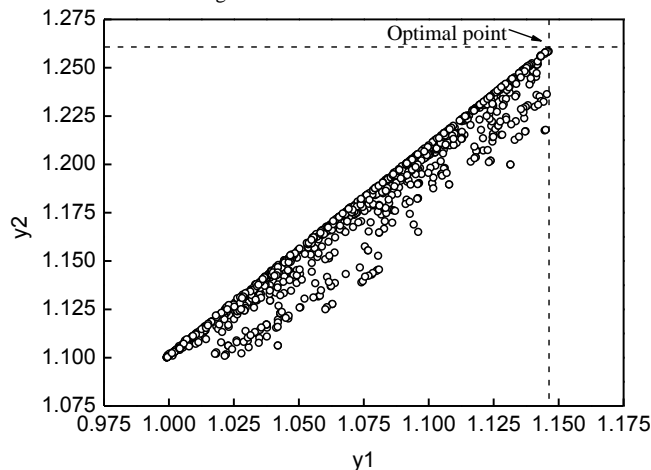

Fig. 17 Flowchart of NSGA-II

Fig. 18 Scatter diagram of Paroto front by NSGA-II

Initial population P(t) is given the number of 100 randomly

and the maximum generation is set to 100. The crossing probability is 0.8. With algorithm searching completed, 10,000 result points which are on behalf of 10,000 solutions are obtained. Similarly, 1467 of those points constitute the Pareto front depicted in scatter diagram shown in Fig. 18.

Similarly, the best solution is summarized in Table VIII.

TBALE VIII BEST SOLUTION BY NSGA-II

Optimization variable	Dimensionless	Real value
b	1.115	4.464
N	1.06	54
e	1.341	1.341
α_p	0.797	0.797

D. Verification for optimization result with FEM

The optimization results produced by the two algorithms and the corresponding simulation results are listed in Table XI.

TBALE XI SIMULATION RESULTS BASED ON THE OPTIMAL SOLUTION BY ALGORITHMS

Algorithm	Results type	T	P
MOPSO	Optimization	-0.667	376.831
	Simulation	-0.588	342.632
NSGA-II	Optimization	-0.668	375.822
	Simulation	-0.594	351.737

On the one hand, it can be apparently seen from Table XI that the breaking torque and generated power optimized with NSGA-II are better than those optimized with MOPSO. On the other hand, the breaking torque and generated power worked out by the two algorithms are closed to those by simulation. It is indicated that the optimization process is correct and reliable.

To further compare the performance indexes between the machine optimized by MOPSO and NSGA-II, simulations for the two kind optimized generators in different revolution speed are carried out, whose the results are exhibited in Fig. 20 which also include the performance requirement such as the 120% times as wind resistance moment. From those figures it can be indicated that the optimization process effectively improve the machine's performance, and furthermore, it can be clearly seen from Fig. 20 that the machine optimized by NSGA-II can output higher breaking torque and generated power than that by MOPSO which can also meet the performance requirement. Therefore, the machine's design parameters are determined by the optimization results with NSGA-II. The geometry parameters' values are listed in Table X.

TABLE X THE MACHINE'S DESIGN PARAMETERS' VALUE BY OPTIMIZATION

Parameter	Determined value
D_o / mm	54
L / mm	14.5
δ / mm	0.1
h /mm	2.65
b / mm	4.464
N	54
e / mm	1.341
α_p	0.797
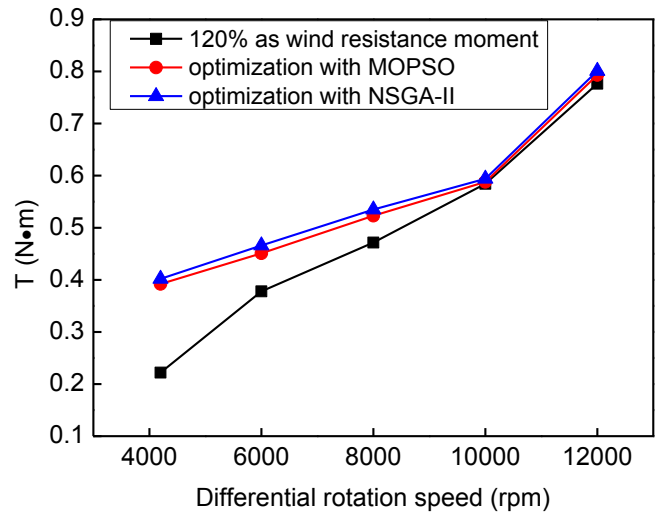
(a) Breaking torque
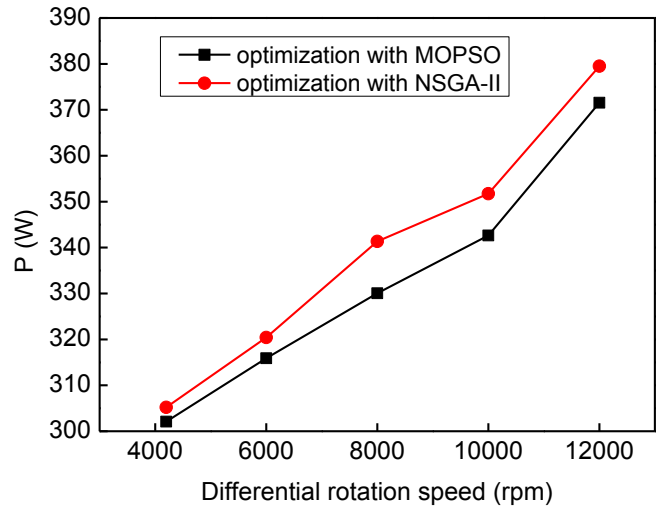
(b) Generated power

Fig. 20 Optimized machine's performance results by simulation in different revolution speed

VI. PROTOTYPE EXPERIMENT

To verify the optimization result, a prototype machine has been manufactured, and experiment is conducted with testing the machine's performance, including breaking torque, generated power. Fig. 21(a) shows the appearance of the prototype machine. High-speed rotating floor exhibited in Fig. 21(b) can test the machine's breaking torque in different revolution speed. The generated power is also measured by multimeter.

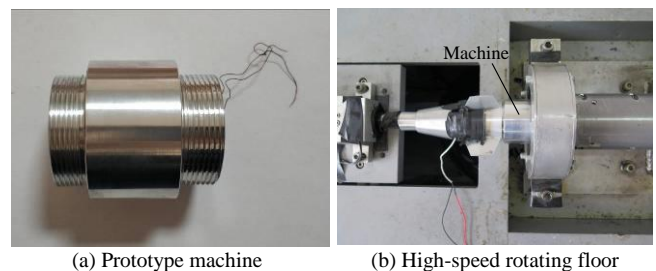(a) Prototype machine   (b) High-speed rotating floor

Fig. 21. Experiment

The experiment results show in Table XI and XII, including the breaking torque and generated power in different revolution speed, respectively. The simulation result of NSGA-II by FEA for the optimized machine, whose the

parameters listed in Table X, also listed in Table XI and XII, to contrast with experiment and verify the simulation results.

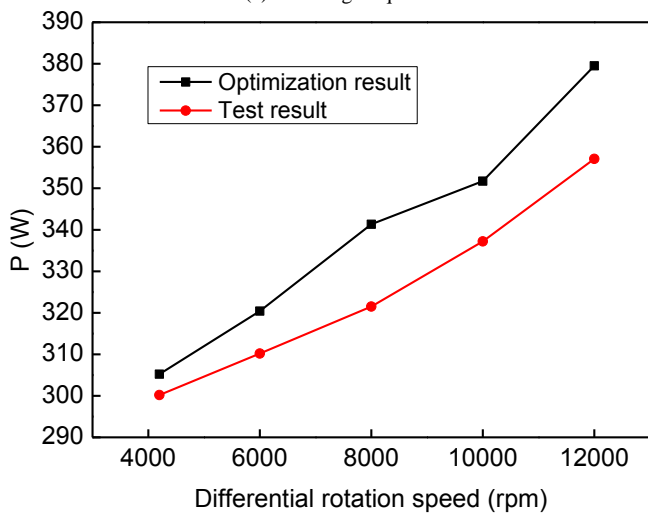TABLE XI GENERATED POWER FROM FEA AND EXPERIMENT

Revolution speed / rpm	FEA result	Test result	Error / %
4200	305.213	300.2	1.7
6000	320.422	310.2	3.3
8000	341.346	321.5	6.2
10000	351.737	337.2	4.3
12000	379.507	357.1	6.3

TABLE XII BREAKING TORQUE FROM FEA AND EXPERIMENT

Revolution speed / rpm	FEA result	Test result	Error / %
4200	-0.402	-0.413	2.7
6000	-0.466	-0.451	3.3
8000	-0.535	-0.52	2.9
10000	-0.594	-0.615	3.4
12000	-0.801	-0.825	2.9
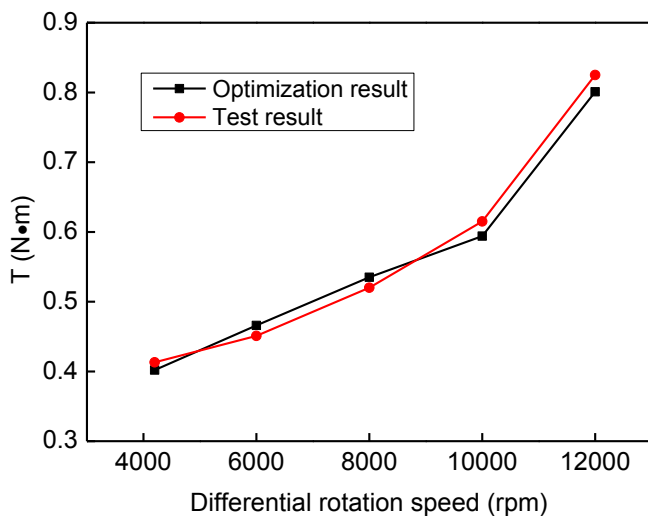
(a) Breaking torque

(b) Generated power

Fig. 22. Tendency of FEA and experiment results

To visualize the contrast between the FEA and experiment results, extracted the data from the two tables, Fig. 22 depicts the tendency of breaking torque and generated power from FEA and experiment with revolution speed increasing. It can be clearly seen that the tendency of experiment result are identical with that of FEA. Besides, the error between the experiment and FEA is no more than 10%, and the results also reach the performance requirement, which verify the correctness of optimization results. The simulation and optimization method are accurate and reliable.

VII. CONCLUSION

As the significant device in the fuze, a novel electrical machine has been proposed and designed for the trajectory correction fuze in this paper. Compared to the traditional machine whose flux path is radial, axial and transverse studied by the researchers and engineers, this kind of machine's flux presents as 3D path. After the proposed machine's topology structure and magnetic equivalent circuit model introduced, to achieve the maximum breaking torque and generated power yielded by machine to effectively ensure the fuze operation during flight, an optimization for the machine's performance have been conducted.

The machine's design parameters determine the machine's performance. The relation between those parameters and performance indexes has been established. Accordingly, the height of rotor teeth, width of stator slot, arc coefficient and winding turns have been served as the optimization variables. Based on the preliminary simulation results and the performance requirement, the machine must be optimized. Therefore, four variables and two objectives constitute the optimization.

In the optimization progress, one of the DOE methods, orthogonal design is used for yielding the sample points based on the four variables and two objectives, the variables effect tendency on the objectives are also obtained with range analysis. Subsequently, three approximation model, RSM, RBF neutral network and Kriging model are created based on the sample points. Kriging model which has the best prediction for the simulation results is selected from the three models with the estimation coefficient. Accordingly, two algorithms, MOPSO and NSGA-II are used to conduct the optimization for the four variables and FEM simulation is also applied to compare the performance indexes between the optimization results from MOPSO and NSGA-II. At last, the optimization result by NSGA-II is better than MOPSO. To verify the optimization results, a prototype experiment is carried out with the prototype machine, and the results indicate the correctness and reliability of simulation and optimization method. The results indicate that the optimization method for the machine is effective and efficient, and also can be a reference for engineers' research about optimization design for electrical machine.

REFERENCES

[1] H. Weh and H. May, "D Achievable force densities for permanent magnet excited machines in new configurations," *Proceedings of International Conference Electronic Machine,* Munchen, Germany, 1986.

[2] A. Masmoudi, A. Njeh, A. Mansouri, et al., "Optimizing the overlap between the stator teeth of a claw pole transverse-flux permanent-magnet Machine," *IEEE Transactions on Magnetics*, vol.40, 2004, pp. 1573-1578.

[3] Y. Guo, J Zhu, PA. Watterson, et al., "Comparative study of 3-D flux electrical machines with soft magnetic composite cores," *IEEE Transactions on Industry Application*, vol.39, 2003, pp. 1696-1703.

[4] C. Liu, J. Zhu, Y. Wang, et al., "Comparison of Claw-Pole Machines With Different Rotor Structures," *IEEE Transactions on Magnetics*, vol.51, 2015, pp. 8110904.

[5] B. Zhang, A. Wang and M. Doppelbauer, "Optimization of a transverse flux machine with claw-pole and flux-concentrating structure," *IEEE*

International Electric Machines & Drives Conference, *Coeur d'Alene*, ID, USA, 2015.

[6] B. Zhang, A. Wang and M. Doppelbauer, "Multi-Objective Optimization of a Transverse Flux Machine With Claw-Pole and Flux-Concentrating Structure," *IEEE Transactions on Magnetics*, vol.52, 2016, pp. 1-10.

[7] I. Hasan, T. Husain, Y. Sozer, et al., "Analytical modeling of a double-sided flux concentrating E-Core Transverse Flux Machine with pole windings," *IEEE International Electric Machines & Drives Conference,* Miami, FL, USA, 2017.

[8] T. Husain, I. Hasan, Y. Sozer, et al., "Design of a Modular E-Core Flux Concentrating Transverse Flux Machine," *IEEE Transactions on Industry Application*, vol.PP, 2018; pp. 1-1

[9] JT. Chen, ZQ. Zhu, S. Iwasaki, et al., "A novel E-core switched-flux PM brushless AC machine," *IEEE Transactions on Industry Application*, vol.47, 2011, pp. 1273-1282.

[10] ZQ. Zhu, JT. Chen, Y. Pang, et al., "Analysis of a Novel Multi-Tooth Flux-Switching PM Brushless AC Machine for High Torque Direct-Drive Applications," *IEEE Transactions on Magnetics*, vol. 44, 2008, pp.4313-4316.

[11] ZQ. Zhu and JT. Chen,, "Advanced Flux-Switching Permanent Magnet Brushless Machines," *IEEE Transaction on Magnetics*, vol. 46, 2010, pp.1447-1453.

[12] C. Lee and R. Krishnan. "New Designs of a Two-Phase E-Core Switched Reluctance Machine by Optimizing the Magnetic Structure for a Specific Application: Concept, Design, and Analysis," *IEEE Transactions on Industry Application*, vol. 45, 2009, pp. 1804-1814.

[13] Z. Jia, H. Lin, H. Yang, et al., "Transverse flux permanent magnet motor with double-C stator hoops and flux-concentrated rotor for in-wheel drive electric vehicle," *IEEE Energy Conversion Congress & Exposition*, Pittsburgh, PA, 2014.

[14] Z. Jia, H. Lin, H. Yang, et al., "A Novel Transverse Flux Permanent Magnet Generator With Double C-Hoop Stator and Flux-Concentrated Rotor," *IEEE Transactions on Magnetics*, vol. 51, 2015, pp.8700704.

[15] J. Yan, H. Lin, Y. Huang, et al., "Magnetic field analysis of a novel flux switching transverse flux permanent magnet wind generator with 3-D FEM," *International Conference on Power Electronics & Drive Systems*, Taipei, Taiwan, 2009.

[16] J. Yan, Q. Li, H. Lin, et al., "Electromagnetic design and analysis of a novel flux-concentrated transverse flux permanent magnet disk generator," *17th International Conference on Electrical Machines & Systems*, Pattaya, Thailand, 2015.

[17] H. Zhang, B. Kou, W. Zhao, et al., "Design and analysis of a bidirectional cross-linking transverse flux permanent magnet synchronous motor," *17th International Symposium on Electromagnetic Launch Technology,* San Diego, Califonia, USA, 2014.

[18] G. Yang, D. Cheng, H. Zhang, et al. "Bidirectional Cross-Linking Transverse Flux Permanent Magnet Synchronous Motor," *IEEE Transactions on Magnetics*, vol. 49, 2013, pp. 1242-1248.

[19] H. Yao, H. Li and K. Wang, "Design and optimization of a concentrated flux transverse flux permanent motor," *IEEE 8th International Power Electronics and Motion Control Conference*, Hefei, China, 2016..

[20] B. Zhang, T. Epskamp, M. Doppelbaue, et al., "A comparison of the transverse, axial and radial flux PM synchronous motors for electric vehicle," *IEEE International Electric Vehicle Conference*, Florence, Italy, 2015.

[21] M. Pinilla, "Performance Improvement in a Renewable Energy Direct Drive Permanent Magnet Machine by means of Soft Magnetic Composite Interpoles," *IEEE Transactions on Energy Conversion*, vol. 27, 2012, pp. 440-448.

[22] G. Nord, R. Jansson, C. Petersen, et al. "Vertical electrical motor using soft magnetic composites," *IEEE International Conference on Electric Machines & Drives*, San Antonio, TX, USA, 2005.

[23] C. Liu, J. Zhu, Y. Wang, et al. "Development of a low-cost double rotor axial flux motor with soft magnetic composite and ferrite permanent magnet materials," *Journal of Applied Physics*, vol. 117, 2015, pp. 17B5071-4.

[24] A. Boehm and I. Hahn, "Comparison of soft magnetic composites (SMCs) and electrical steel," *2nd International Electric Drives Production Conference*, Nuremberg, Germany, 2012.